World Electric Vehicle Journal

MDPI

Article

Influence of Adhesive Tapes as Thermal Interface Materials on the Thermal Load of a Compact Electrical Machine

Henrik-Christian Graichen [1,*], Jörg Sauerhering [2], Olena Stamann [3], Frank Beyrau [1] and Gunar Boye [1]

[1] Institute of Fluid Dynamics and Thermodynamics, Otto von Guericke University Magdeburg, 39106 Magdeburg, Germany; frank.beyrau@ovgu.de (F.B.); gunar.boye@ovgu.de (G.B.)
[2] Department of Applied Biosciences and Process Engineering-Thermal Process and Energy Engineering, Anhalt University of Applied Sciences, 06366 Köthen, Germany; joerg.sauerhering@hs-anhalt.de
[3] Institute of Materials and Joining Technology, Otto von Guericke University Magdeburg, 39106 Magdeburg, Germany; olena.stamann@ovgu.de
* Correspondence: henrik.graichen@ovgu.de; Tel.: +49-391-67-58575

Abstract: In this article, a novel form of thermal interface material (TIM), represented by three industrially manufactured pressure-sensitive adhesive (PSA) tapes with electrical insulating properties, is characterized regarding its applicability in an electric motor with air-gap winding. Firstly, the adhesion performances, in terms of the winding process, were investigated experimentally. Here, every TIM shows sufficient shear strength for the wire–TIM joints, as well as peel adhesion to the laminated iron core. Secondly, the thermal–physical properties of the TIMs are inspected experimentally via laser flash analysis (LFA) and differential scanning calorimetry (DSC). For every TIM, the value of the thermal resistance can double if the relatively smooth surface (R_a = 0.2 µm) of the adjacent layers is interchanged with a rougher one (R_a = 2.0–3.7 µm). Additionally, the TIM's performance at the system level is examined. Therefore, a flat test section, according to the specifications of the original motor, is studied experimentally and numerically utilizing infrared (IR) thermography and the finite element method (FEM). The focus is set on the heat flow and temperature distribution in the test section under varying thermal loads, mass flow, and variety of TIMs.

Keywords: electrical actuators; liquid cooling; FEM simulation; IR-thermography; thermal analysis; thermal interface materials

check for updates

Citation: Graichen, H.-C.; Sauerhering, J.; Stamann, O.; Beyrau, F.; Boye, G. Influence of Adhesive Tapes as Thermal Interface Materials on the Thermal Load of a Compact Electrical Machine. *World Electr. Veh. J.* **2022**, *13*, 42. https://doi.org/10.3390/wevj13020042

Academic Editor: Zi-Qiang Zhu

Received: 23 November 2021
Accepted: 16 February 2022
Published: 19 February 2022

Publisher's Note: MDPI stays neutral with regard to jurisdictional claims in published maps and institutional affiliations.

Copyright: © 2022 by the authors. Licensee MDPI, Basel, Switzerland. This article is an open access article distributed under the terms and conditions of the Creative Commons Attribution (CC BY) license (https://creativecommons.org/licenses/by/4.0/).

1. Introduction

An increased power-to-mass ratio is highly demanded in mobile applications, such as automotive and aviation cases. Electric motors applying an air-gap winding, as shown in Figure 1, can achieve these demands through minimization of the acquired iron mass [1]. Considering a 16" diameter, large, 20 kg heavy motor with a mechanical output of 80 kW and a thermal loss of 10%, the heat losses due to dissipation from the cooling fluid can reach 8 kW [2]. The restrictions here mostly result from the thermal limitations of the applied materials by the Joule heating in the motor's winding. To guarantee long-term reliability and optimum performance of the machine, it is essential to establish proper thermal management. The heat must be spread out from its source, the winding, to the heat sink, namely the cooling channels (CCs). Inside solids, conduction embodies the dominant heat transport mechanism and multiple layers with conforming surfaces have to be crossed by the transported heat (see Figure 2).

Contact resistances at the solid–solid interfaces inhibit heat dissipation since the surfaces contact each other only in a small percentage of the nominal area, which is due to surface roughness and undulations [3,4]. Only in areas with actual mechanical contact can a conductive heat transfer path emerge. This leaves gaps filled with air, in which the thermal conductivity is smaller by orders of magnitude, and results in a significant temperature jump across the solid contact interface (see Section 2). For decades, TIMs have been widely

used as filler materials in applications of micro- and power electronics to reduce thermal contact resistance [5–8]. Common types of TIMs are thermal greases, polymeric phase change materials (PCMs) in the form of thermal pads, filled and unfilled polymers in the form of films, low melting alloys (LMAs), and, in the recent past, carbon-nanotube-based materials [5,8–10].

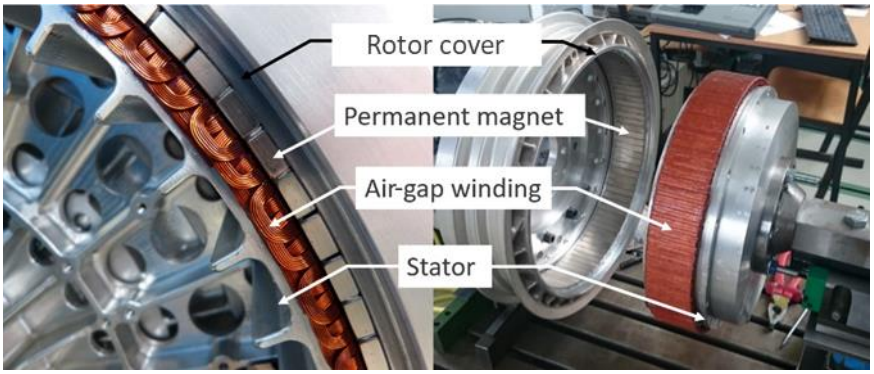


Figure 1. Basic structure of an electric machine with an applied air-gap winding.

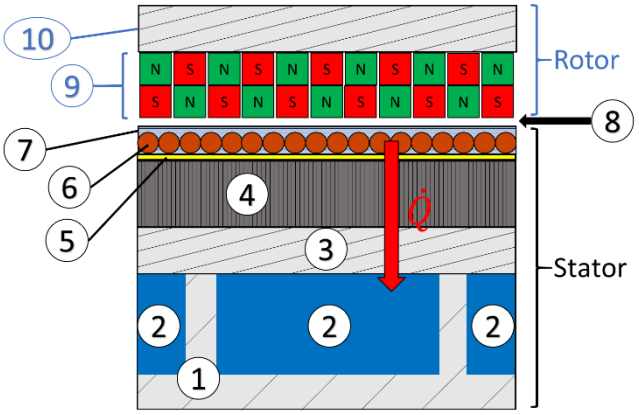


Figure 2. Structure of the stator and the inner rotor; visualization of the heat dissipation (1—stator base body, 2—cooling channels, 3—cover ring, 4—laminated iron core, 5—TIM, 6—winding, 7—bandage of glass fiber and resin, 8—air-gap, 9—permanent magnets, 10—rotor cover).

Regarding the ability to reduce thermal interface resistance, two factors are of dominating significance: the thickness and thermal conductivity of the TIM itself, and its potential to wet the adherent surfaces to reduce contact resistances [8,11]. Grujicic et al. identify two categories of TIMs [11]. On the one hand, paste-like greases, gels, adhesives, and PCMs with rapidly decreasing viscosity at higher temperatures have outstanding gap-filling properties. Meanwhile, asperity-induced micro-contacts persist and promote heat conduction. Yet, the heat conductivity of these TIMs is rather low. On the other hand, polymer-based thermal pads and films show a slightly higher thermal conductivity, especially when particle-laden (filled) with conductive materials. However, these materials prevent micro-contacts by building a physical barrier between the mating surfaces. Additionally, they show a substantially smaller capability of surface wetting and tend to increase interface thicknesses by a larger margin.

Despite the improved heat transfer across the solid–solid interface, TIMs still contribute most of the system's thermal resistance [12]. Consequently, the development and fabrication of high-performance TIMs is still a current topic of research [9,10], as researchers gain a better understanding of thermal contact resistances and energy transport mechanisms at the interface [13]. Additionally, the impact of boundary conditions on TIM thermal behavior has been thoroughly examined. Zhao et al. showed extensive results of how

surface roughness, temperature, and pressure affect the interface thermal resistance of the common TIMs mentioned above [14].

The design process of application-specific TIMs often solely regards thermophysical properties. Cui et al. identified the future need to consider multi-physical material properties in research (thermal, mechanical, electrical, or optical nature) to meet the needs of more complex applications, and to develop urgently needed advanced materials [13].

As Figure 2 shows, electric motor applications make use of an air-gap winding that relies on adhesive bonding during manufacturing, in comparison to slot windings, where mechanical fixture is achieved by clamping coils within the slots.

Copper wires are applied and have to be fixed without detachment until a permanent bandage of glass fiber and resin is applied during the next manufacturing step. The completion of the winding process can take up to 72 h. Another requirement arises with copper wires operated at high voltage levels. Therefore, sufficient electrical insulation is also essential to prevent electrical breakdown. Due to the analogy of heat and electricity transport, a trade-off between the mandatory electrical insulation of the source and minimal thermal resistance towards the sink has to be solved. Common TIMs cannot fulfill these multi-criteria requirements of electric insulation and adhesive effect while maintaining a decent heat conductivity. As described before, common grease-like TIMs do not guarantee electrical insulation due to micro-contacts. In addition, side effects like pump-out, phase separation, or dry-out occur during their lifetime [15,16]. Common film-like TIMs have little to no wetting capabilities, resulting in increased thermal resistance, and do not possess any adhesive effect.

Pressure-sensitive adhesive tapes (PSAs) can meet all of the three requirements—electric insulation, adhesion, and heat transport—depending on the materials used. The concept itself is widespread and its utilization as flexible packaging tape in transportation, as athletic tapes in the healthcare industry, or as insulating tape used daily by electricians, show its versatility. Due to their multi-functionality, low cost, and ease of use, PSA-based TIMs are increasingly being used in electronic applications for long-lasting heat sink attachments [8,17–23].

However, scientific examinations of thermal properties regarding PSA-based TIMs, especially under the influence of varying boundary conditions, such as surface roughness and temperature, are rare.

Chirtoc et al. experimentally examined the thermal resistance of four different adhesive tapes using a photoelectric method. Exact information about the composition of the samples and the roughness variation was not provided, as the focus was on the sensor system [24].

Chu et al. stated that vendor data do not often fit the results that are obtained from actual applications. Therefore, they examined PSA-based TIMs from three different manufacturers from the point of view of thermal performance with a self-build test setup, which consisted of a heater and a fan heat sink, with TIMs installed between them. Resistance temperature detectors (RTDs) were used for temperature measurements. The sensitivity of adhesive curing, the effect of the surface flatness (one machined flat test head and one with a concave curvature were used), the TIM thickness, and the variations in power density were considered. Deviation from the manufacturer's data was shown, but the composition of the samples and the influence of roughness were not provided [22].

Hienonen et al. focused on the reliability of diverse TIMs used in electronics. Among others, PSA-based tapes were measured using the HotDisk® method, but the authors describe the method as not suitable for heat conductivity measurements of thin films [25]. Additionally, thermal impedance was measured in terms of ASTM D5470-01 standard. This is the standard test method for thermal transmission properties of thin thermally conductive solid electrical insulation materials. The repeatability of this method is rather low and it is therefore criticized.

Demko et al. examined multiple properties of three thin electrically insulating TIMs [26]. The thermal conductivities were determined using an instrument that was also based on the ASTM D5470 standard. They could show the increase in thermal conductivity

of filled polyimides compared to unfilled ones by up to four times with remaining dielectric breakdown strength. They also examined one polyimide film with and without applied pressure-sensitive adhesives and showed the adhesive's effect on the interfacial thermal resistance. A smooth glass surface can be contacted significantly better due to increased wetting abilities of the adhesives, but behavior regarding rough surfaces remains unclear.

This paper will address mechanical and thermal property examinations of PSA tape combinations with a special focus on the heat transport capability at different surface roughnesses of the adjacent materials. Since TIM application performance in a motor's stator is of utmost interest, the influence of different adhesive tape combinations on the thermal behavior of the electrical engine is discussed.

To achieve this, strength tests with a material testing machine are performed with the TIMs. If sufficient adhesive performance can be reached, according to the requirements of the winding process, thermal–physical properties are determined using different measurement techniques. DSC is applied to determine the specific heat capacity and LFA is used for the thermal diffusivity.

The results are comparatively discussed and enable the establishment of a detailed FEM-based model of the stator to predict the influence of different TIMs on its thermal behavior. The fabrication of the stator is of high complexity and the stator has limited accessibility for measurements of an optical nature. Therefore, a flat test section that consists of an electrically heated surface, the TIM and the base-body structure with the included cooling ducts, is experimentally investigated under application-oriented boundary conditions. Here, the hydraulic characteristics are examined and the surface temperature is measured utilizing infrared thermography. Since the heat and mass transfer inside the test section is modeled using FEM, it can be compared to the experimental results conducted at the test rig.

In general, this paper examines the applicability and suitability of PSA tapes as TIMs regarding multi-criteria requirements of thermal and mechanical nature in a compact electrical machine.

2. Data Reduction

The temperature difference, ΔT, as shown in Equation (1), between the heat source (winding) and heat sink (cooling duct) depends on heat flux $\dot{q}$, as well as the overall effective unit of heat transfer (u_{eff}) or the thermal resistance (r_{th}) as its reciprocal value, respectively [27].

$$\dot{q} = \frac{\dot{Q}}{A} = u_{eff} \cdot \Delta T = r_{th}^{-1} \cdot \Delta T \quad (1)$$

The overall resistance itself can be calculated, assuming a series connection of single thermal resistances, starting from the convective heat transfer inside cooling ducts h_{cd} and through all layers, i, in between the source and the sink, with layer thickness s and layer thermal conductivity k. Here, Equation (2) shows an ideal case, where contact resistances can be neglected.

$$r_{th} = \frac{1}{h_{cd}} + \sum_{i=1}^{n} \frac{s_i}{k_i} \quad (2)$$

The single resistance with the highest magnitude results from the adhesive and electrical insulating TIM between the meander-shaped windings and the stator's laminated iron core.

As Figure 3 can show, the overall thermal resistance of the TIM r_{TIM} is composed as a resistance network out of three resistances in series, where r_{c1} and r_{c2} embody the contact resistances between the adhesive and both adjacent layers and r_{bulk} the bulk resistance of the TIM material (Equation (3)) [28].

$$r_{TIM} = r_{c1} + r_{bulk} + r_{c2} \quad (3)$$

The schematic interface section shown here is similar to the samples examined regarding the thermal–physical properties, see Section 5.

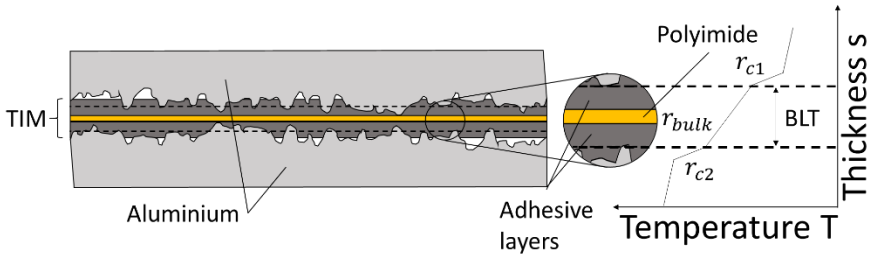


Figure 3. Schematic interface section of two conforming rough surfaces with the implementation of an adhesive tape as a TIM.

As adhesive tapes are composed of three layers, the bulk resistance, in reality, is even more complex (Equation (4)), see also Section 3. Heat is transported through two adhesive layers and the polyimide film. Additionally, two additional contact resistances emerge at the interfaces inside the TIM. Whereas, the bulk resistance of a homogenous TIM solely depends on the bond line thickness (BLT) and the heat conductivity of the TIM k_{TIM}, see Equation (5).

$$\text{Inhomogeneous}: \; r_{bulk} = \frac{s_{adh,1}}{k_{adh,1}} + r_{c1,\,TIM} + \frac{s_{pi}}{k_{pi}} + r_{c2,TIM} + \frac{s_{adh,2}}{k_{adh,2}} \tag{4}$$

$$\text{Homogeneous}: \; r_{bulk} = \frac{BLT}{k_{TIM}} \tag{5}$$

In the following, we will treat the TIMs as a thermally homogeneous medium, for which the reasons are as follows:

1. The available adhesive tape samples were industrially manufactured and were delivered ready to apply. Peeling off the adhesives causes structural damage to the polyimide film. An examination of the thermal–physical properties is hardly possible.
2. The application of the TIMs and their overall heat transfer performance is of utmost interest. Measurement by LFA includes every contact resistance into an effective heat conductivity k_{eff} and is therefore technically reasonable. In addition, the influence of roughness can be observed here.

Equations (3)–(5) simplify to Equation (6):

$$r_{TIM} = r_{c1} + \frac{BLT}{k_{TIM}} + r_{c2} = \frac{s_{TIM}}{k_{eff}} \tag{6}$$

3. Materials

The investigated materials are composed as a three-layer TIM of two adhesive layers and a polyimide film as the carrier.

Kapton® polyimide films are widely used for various applications in electrical engineering, e-mobility, power electronics, aerospace engineering, cooling of lithium-ion battery packs, etc. For slot windings, oil-impregnated aramide paper and more advanced materials like NOMEX® are in common use.

To achieve an optimized thermal conductivity of adhesive TIMs, both the adhesive and the carrier are provided with appropriate additives, such as conductive fillers (e.g., ceramic-based or aluminum oxide). In this study, three pressure-sensitive laminated adhesive film combinations are analyzed concerning their mechanical and thermal behaviors, see Table 1.

Table 1. Investigated adhesive tape combinations.

	Adhesive 1 (Wire-Side)	Carrier (Thickness, Dielectric Strength)	Adhesive 2 (Stator-Side)	Total Thickness
TIM 1	Standard acrylate 50 µm	Kapton® HN 12.7 µm 315 kV/mm	Heat conductive acrylate 20 µm	82.7 µm
TIM 2	Standard polysiloxane 40 µm	Kapton® MT+ 25 µm 213 kV/mm	Heat conductive polysiloxane 20 µm	85 µm
TIM 3	Standard acrylate 50 µm	Kapton® CR 25 µm 236 kV/mm	Standard acrylate 30 µm	105 µm

Three different polyimide films with sufficient dielectric strength requirements (breakdown voltage for the studied electric machine $\geq$3 kV) for reliable insulation were selected as carriers. In addition to general-purpose Kapton® HN, further tape formulations with optimized properties were tested as TIM. Kapton® MT+ is one of the latest developments in polyimide films and is characterized by its manufacturer by more than three times the thermal conductivity due to the special fillers in the carrier. The other carrier type Kapton® CR has an improved partial discharge resistance due to the filler content, which guarantees a 20 times higher durability than that of standard polyimide film. The investigated film carriers were used in the lowest available film thickness (12.7 µm or 25 µm) to achieve the requirement of the minimum possible total layer thickness of the PSA tape.

The composition of the laminated adhesives on both sides of the TIMs differed. They were adapted to ensure optimal adhesive strength of the winding attached to the stator with the best possible heat dissipation. A thick adhesive layer enables the fixture of the winding, while a thinner heat conductive layer is adequate to attach the polyimide carrier to the laminated iron core. Standard acrylate, polysiloxane and filled heat conductive acrylate- and polysiloxane-based adhesive coatings were combined on the film carriers and tested concerning their adhesive strength suitability and their influence on the entire laminated tape. Generally, acrylates are characterized by a very good adhesive strength, while polysiloxane adhesives have the highest temperature resistance and extreme resistance to aging. The manufacturer guarantees the uniform application of the adhesives to the substrate, entirely without any inclusions to ensure the electrical requirements.

Concluding, the non-flexible pressure-resistant Kapton® polyimide film ensures dielectric strength. Additionally, the thin gap-filling adhesive coatings on the carrier generate the TIMs' wetting potential and therefore reduce the overall thermal resistance [29,30].

4. Mechanical Properties

The Zwick/Roell Z2.5 materials testing machine with a maximum test load of 2.5 kN and the testXpert® software were used for the strength tests. To evaluate the adhesive strength of the winding to the TIMs' adhesive layers, tensile shear tests were conducted. The examinations were carried out on the wire pack adhesive bonds with TIMs at room temperature, according to DIN EN 1465 (see Figure 4).

Here, the adhesive strength of the wire pack to either the acrylate-based or the polysiloxane-based adhesive layers can be compared. The properties of adhesive performance determined here are needed during the winding process until a permanent bandage is applied. Specifically, the required resistance of the wire pack adhesive bonds against potential shear stress is determined. A conditioning time of the joints of at least 24 h should be ensured. This way, the initial adhesive strength of the wire pack-TIM joints can be estimated here.

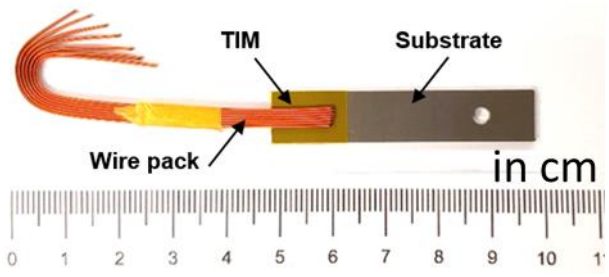


Figure 4. Wire pack adhesive bonds for a tensile shear test.

A tensile force of approx. 30 N acts on the wire winding in the axial direction during the winding process. This was specified as a required strength criterion. Accordingly, tensile shear strength of approx. 0.09 MPa is required for the windings' adhesion, with the tested wire size of 0.42 mm × 0.6 mm.

The results show that the shear strength of every TIM's adhesive film (acrylate- and polysiloxane-based) to the wire winding is sufficient, during the winding process with the existing winding equipment, see Table 2 [31].

Table 2. Investigated adhesive strength of adhesive layers of TIMs (n = 5) and mechanical properties of Kapton®-film carriers; standard deviation σ is given in brackets.

	Adhesive 1 (Wire-Side) Shear Strength MPa at 23 °C	Carrier Tensile Strength [1] MPa at 23 °C	Adhesive 2 (Stator-Side) Peel Adhesion N/20 mm at 130 °C
TIM 1	1.05 (0.15)	231	2.98 (0.98)
TIM 2	0.96 (0.11)	76	3.61 [2] (0.51)
TIM 3	1.05 (0.15)	152	6.28 (1.92)

[1] According to the datasheet. [2] Pre-treated with Primer 94 by 3M™.

For the application and further processing of the investigated PSA-based TIMs on the laminated iron core, the adhesive strength of the adhesive layers to the metallic substrate also had to be determined. Here, it was important to evaluate the adhesion at the expected maximum operating temperature of about 130 °C. The samples for the peel test were prepared according to DIN EN ISO 8510-2. Their dimensions were scaled down to a width of w_{sample} = 0.02 m and a length of l_{sample} = 0.1 m with a peel length of 0.055 m. Eighty-grit sandpaper was used to generate a roughness of R_a = 1.2 µm on the rigid substrate. This adapted approximately to the surface condition of the laminated iron core, after turning, and before bonding (R_a = 1.4 µm). To ensure the adhesive strength of the TIMs' stator-side adhesive layers at the operating temperature, the bonded joints were heated during the test. A temperature-controlled hot air blower was used. The test setup with a stressed sample in the 180-degree peel test is shown in Figure 5.

The required adhesion strength of the TIMs on the stator can be estimated by accomplishing the strength criterion. It is based on the Lorentz force F_L responsible for the rotation of the rotor. Corresponding electrical parameters of the investigated machine have to be considered for the resulting effective Lorentz force—the stator width w_{stator}, the peak current I_{max}, and the maximum magnetic flux density B_{max}. The effective Lorentz force of 32 N acting on a phase conductor is obtained, see Equation (7).

$$\begin{aligned} F_L &= B_{max} \cdot w_{stator} \cdot I_{max} \\ F_L &= 1.28\ \mathrm{T} \cdot 0.1\ \mathrm{m} \cdot 250\ \mathrm{A} = 32\ \mathrm{N} \end{aligned} \quad (7)$$

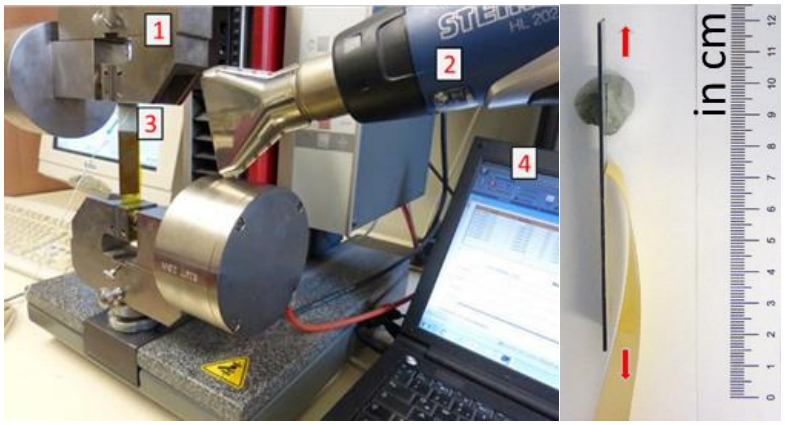


Figure 5. Setup of the 180-degree peel test (1—tensile testing machine Zwick 2.5, 2—hot air blower, 3—tested sample with type K thermocouple, 4—laptop for temperature measurement and control).

The bonded wire pack consists of six copper wire conductors, which corresponds to one winding phase of the electrical machine described here. Under the assumption that the wire pack is securely connected to the TIM, the acting peeling force is concentrated exactly on the wire at the edge of the pack. This results in a minimum required peel strength, $F_{peel,min}$, of 1.07 N/20 mm for the tested samples, see Equation (8).

$$F_{peel,min} = \frac{F_L}{6 \cdot l_{stator}} = \frac{32\ N}{6 \cdot 0.1\ m} = 1.07 \frac{N}{20\ mm} \quad (8)$$

Results of the test show, see Table 2, that the peel forces of the examined TIMs reach higher values than the minimum required peel strength.

The filled acrylate and polysiloxane-based adhesive formulations provided a lower peel strength to the substrate than the standard acrylate coating, see Tables 1 and 2. This is based on the extra-thin adhesive layers and the filler contents therein. To increase the adhesion of TIM 1 and TIM 2, the manufacturer recommended to preheat the substrate up to approx. 60–80 °C.

However, it was found that the low adhesive strength of the polysiloxane coating of TIM 2 to the untreated substrate could cause problems during processing and operation. For industrial use, it is recommended to pretreat the substrate with a special primer to increase the weak adhesion of the adhesive coating. The use of primer in the application of TIM 2 samples resulted in a higher initial adhesive strength and sufficient peel strength to the substrate.

As expected, the samples with a standard acrylic adhesive coating (TIM 3) showed a high value of peel strength in comparison. However, a lower reproducibility of the bonded joints was observed. Because of the high strength to the substrate, TIM 3 can be used for the winding process without further chemical pre-treatment of the stator surface.

5. Thermal-Physical Properties

To evaluate the thermal-physical properties of the different TIMs, these were examined utilizing laser flash analysis, Netzsch LFA 427. In a real bond, different contrary phenomena can occur, e.g., the reduction of contact resistances by adapting the TIM to the roughness profile of the parts to be joined or the increase of thermal resistances due to defects, as would be expected with air inclusions. To take this into account, the TIMs' thermal–physical properties were investigated in the applied state as a three-layer analysis. The structure of the test samples is shown in Figure 6. The samples have a diameter of 12.5 mm and a total thickness of about 6 mm. Adhesives and film carriers have a variable thickness, depending on the sample, as shown in see Table 1. Here, the TIM is considered as a homogeneous layer with an effective thermal conductivity determined for it, see Equation (6). Among

others, Refs. [32,33] showned that LFA provides reliable values for the investigation of multilayer structures and the investigation of contact resistances, even of very thin layers.

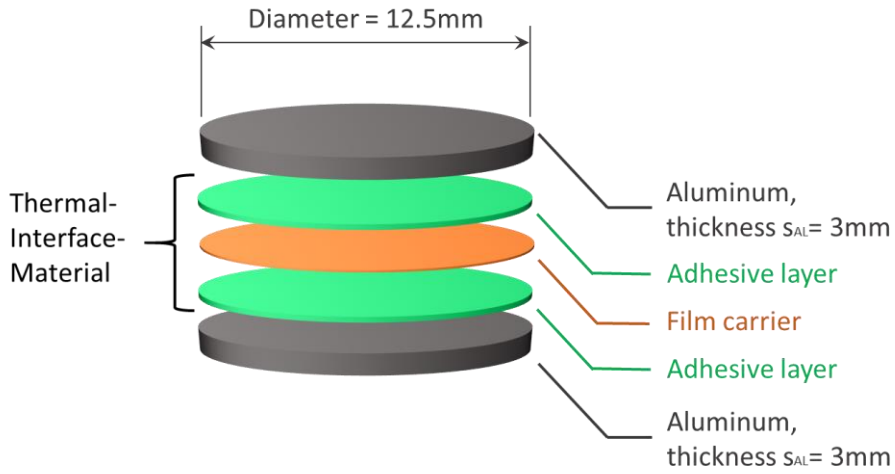


Figure 6. Structure of the LFA multilayer samples.

Since, in the application, the TIM was used to fixate the winding on the relatively rough laminated iron core package, the effect of roughness was also investigated. For this purpose, two samples with a relatively smooth surface of R_a = 0.2 µm and two samples with a relatively rough surface of R_a = 2.9–3.7 µm were measured for each TIM, listed in Table 1. The surface of the aluminum alloy was roughened using 80-grit sandpaper. The generated roughness corresponds approximately to the values of the real laminated iron core package after turning and grinding. The smooth surface corresponds to the values of the flat test section introduced later in Section 6.

To obtain precise values of the TIM in the middle of the lamination, it is necessary to determine the thermal-physical properties of the aluminum alloy, in addition to the geometric dimensions of the three layers. For this purpose, density ρ was determined by means of a dilatometer, Netzsch DIL 402 C, specific heat capacity c was determined by means of a differential scanning calorimeter, Netzsch DSC 404 C Pegasus, and thermal diffusivity D was determined by means of laser flash analysis as a function of the sample temperature. To reduce reflections and, thus, improve the measurement signal during the laser flash measurements, the samples were coated with graphite spray.

Utilizing all the measurements carried out, thermal conductivity k could be determined with Equation (9). The results of the analysis of the aluminum alloy are listed in Table 3.

$$k(T) = D(T) \cdot \rho(T) \cdot c(T) \quad (9)$$

Table 3. Thermophysical properties of the aluminum alloy.

Temperature in °C	Heat Capacity in J/(kgK)	Density in kg/m^3	Th. Diffusivity in mm^2/s	Th. Conductivity in W/(mK)
25	910	2664	60.505	146.6
50	913	2661	61.466	149.3
75	915	2657	62.290	151.4
100	920	2652	62.718	152.9
125	919	2646	63.294	154.0

To evaluate the thermal–physical properties of the TIM using Equation (9), the density was calculated from the volume, based on the geometric dimensions, and the mass, determined using an analytical balance. The specific heat capacity was determined for all TIMs using DSC with a heating rate of 10 K/min under atmospheric conditions. For this purpose, several layers of a TIM were bonded into the aluminum crucible. The results of

these measurements are given in Table 4. The uncertainty was reported for a confidence level of C = 95%.

Table 4. Specific heat capacity of all investigated TIMs in J/(kgK).

Temperature in °C	30	50	75	100	130
TIM 1	1722 ± 225	1774 ± 53	1847 ± 56	1902 ± 47	1979 ± 60
TIM 2	1290 ± 163	1319 ± 43	1362 ± 42	1390 ± 32	1437 ± 44
TIM 3	1668 ± 221	1710 ± 47	1777 ± 52	1814 ± 44	1883 ± 56

To verify the statistical significance of the LFA measurements, two samples were measured at three cycles for each TIM and for every roughness variation. Every cycle consisted of five individual measurements at each temperature level, as shown in Table 3.

In Figure 7, the mean values of the determined thermal conductivity are shown exemplarily for each sample of TIM 2. It can be seen that the influence of the sample temperature plays a minor role on the thermal conductivity. In contrast, a clear effect can be seen when comparing smooth and rough surfaces of the aluminum alloy. For example, an increased roughness leads to a halved thermal conductivity, which can finally be explained very well by the inclusion of micro air bubbles and the associated increased thermal resistance, see Figure 3. Furthermore, it can be seen that this effect is much greater than the random deviation of two samples with identical roughness properties, see Figure 7. The variation of the measured values was higher for the rougher samples, which can be attributed to the range of roughness values, R_a = 2.9–3.7 µm, produced with the sandpaper.

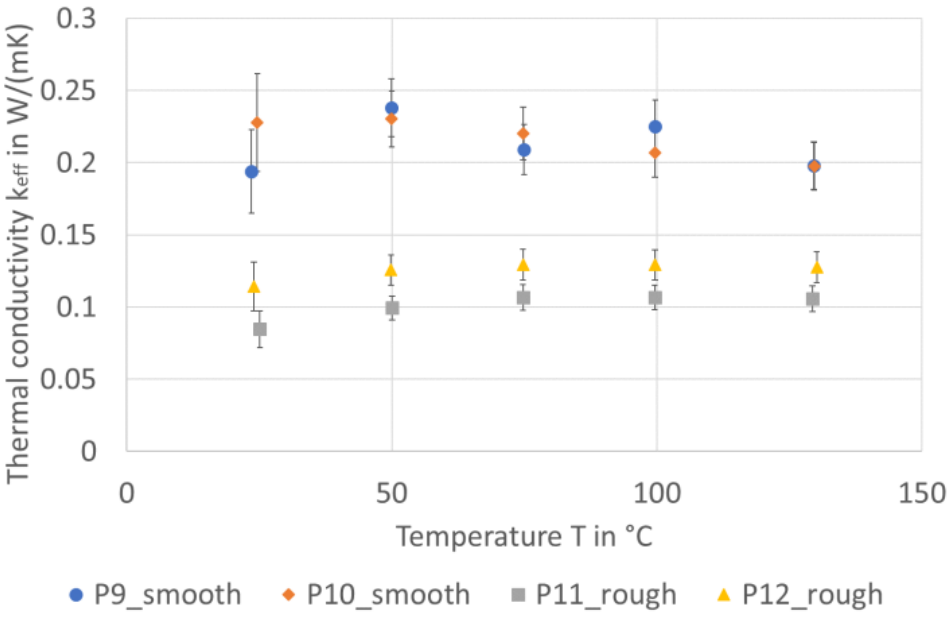


Figure 7. Thermal conductivity of TIM 2 as a function of temperature.

To evaluate the performance of individual TIMs with different roughness values of the joining surfaces, the respective layer thicknesses must be compared in addition to the effective thermal conductivity (see Equation (6)). For this purpose, the thermal resistances of both corresponding samples with similar roughness are averaged in Figure 8. For all investigated TIMs, the thermal resistance increased by a factor of up to two if the surface was rough. This effect was dominant, compared to the variation of the TIMs, and showed that smooth joining surfaces are essential to reduce the thermal resistance, which can be well explained by a better wetting of the roughness profile.

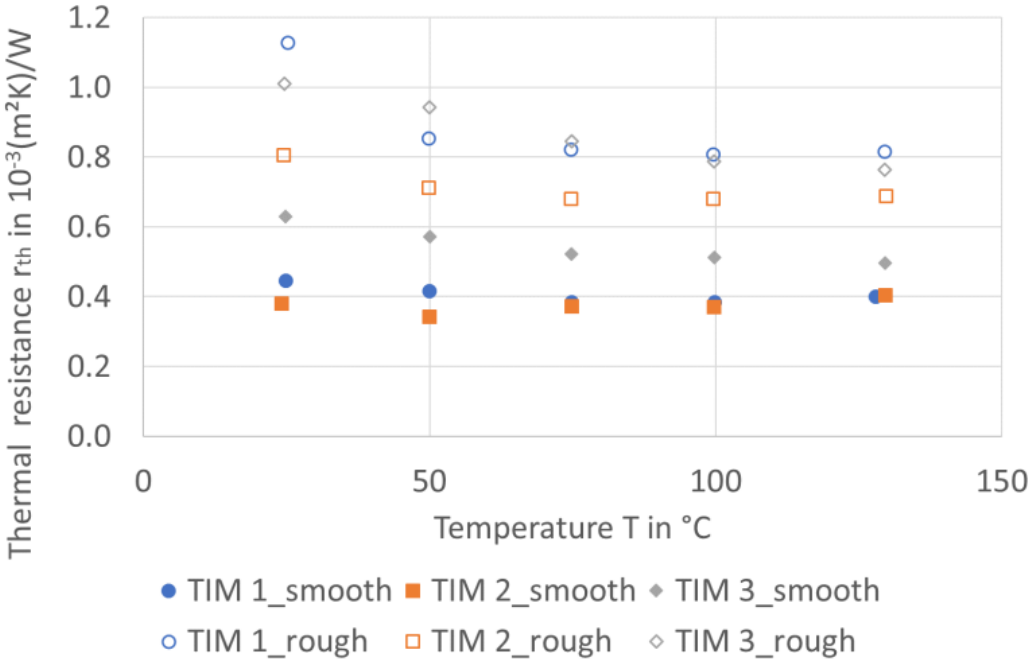


Figure 8. Average thermal resistance of every investigated TIM.

Comparing the deviations of the thermal resistances for smooth samples, it can be seen that TIM 1 and TIM 2 provide almost similar values. This is remarkable, as both TIMs have approximately the same total thickness and the carrier layer of TIM 2 has a significantly higher thermal conductivity, see [26]. TIM 3 shows the highest thermal resistance in terms of smooth samples. For this, the lower thermal conductivity of the adhesive layers could be responsible, in addition to the larger overall thickness.

Regarding the rough samples, also TIM 2 indicates the lowest thermal resistance. The respective values for TIM 1 and TIM 3 only show differences in the lower temperature range. The results suggest that the acrylate adhesives used are wetting the surfaces of the rough samples less effectively than the polysiloxane adhesives of TIM 2 and, thus, generate a higher contact resistance.

Despite the higher total thickness of TIM 3, the thermal resistance compared to TIM 1 is still of the same size. This can indicate a contact resistance decrease of higher adhesive layer thicknesses in combination with rough surfaces.

In [34], a material similar to TIM 2 with a slightly thicker adhesive layer on both sides (20 µm → 40 µm) is presented. Here, the effective thermal conductivity is no longer a function of the chosen surface roughness variation. This degree of freedom in the choice of roughness is coupled with a higher thermal resistance of the TIM in general, due to a larger total thickness. In terms of magnitude, the thermal resistance of the TIM achieves medium values, which means that TIMs with thinner adhesive layers perform better in combination with smooth adjacent surfaces and worse with rough ones.

Optimization of adhesive layer thickness regarding the respective surface roughness is a future task that holds improvements for increasing the heat transfer.

Overall, it can be summarized from these investigations that TIM 1 and TIM 2 have the lowest thermal resistance with smooth joining partners, whereby this advantage decreases at higher temperatures. It is assumed that the mentioned fillers in combination with the low total thicknesses are largely responsible for this behavior.

The measurement uncertainties of the thermal conductivity u(k_{eff}) are given in Figure 9 for all TIMs investigated. For this purpose, the Gaussian error propagation law was applied to Equation (9).

The fraction of measurement inaccuracies of the density determination is between 7% and 9%, due to the small thickness and weight of the TIM.

Regarding the determination of the specific heat capacity, an equipment specific uncertainty (ESU), a model specific uncertainty (MSU), and a sample specific uncertainty (SSU) are considered as contributors to the combined standard uncertainty of the measurement result. Within a wide measurement range, the uncertainties are below 3%. Only in the lower temperature range do the uncertainties increase to 16%.

The uncertainties in the determination of thermal diffusivity are assumed to be 3% of the measured value for multi-layer measurements, according to the manufacturer's specifications.

These observations show that the measurement uncertainty of the thermal conductivity is strongly influenced by the density determination and that, only in the lower temperature range, the measurement uncertainty of the specific heat capacity becomes dominant.

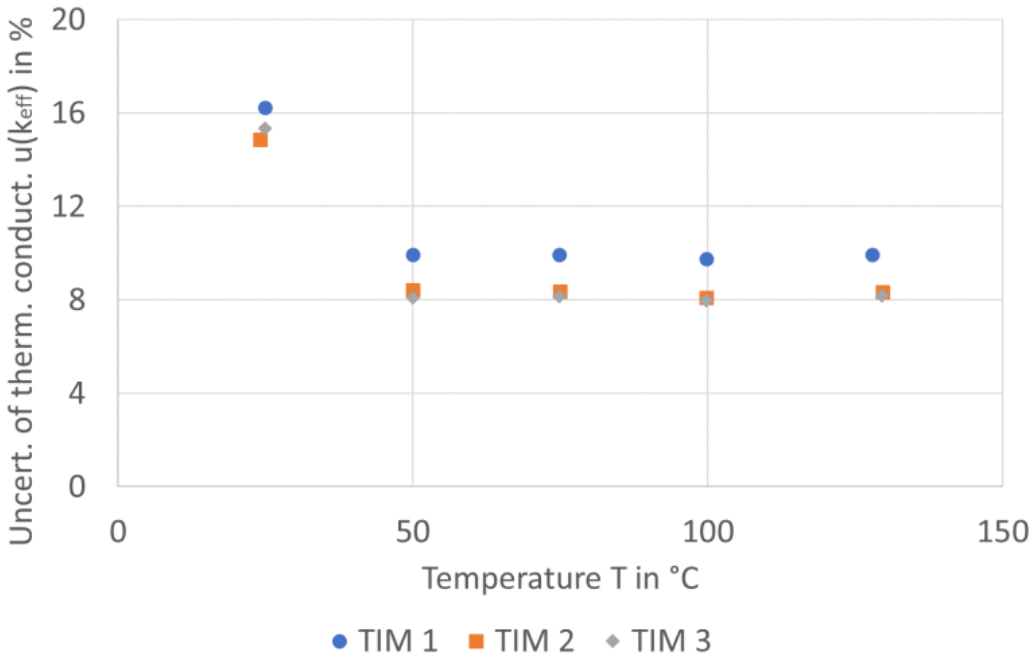


Figure 9. Uncertainty of thermal conductivity regarding every investigated TIM.

6. Comparative Numerical and Experimental Investigation in a Flat Test Section

To obtain the thermal behavior of the TIMs under engine-like conditions, a comparative numerical and experimental study was conducted. To achieve this objective, the surface temperature of the ohmic heated windings had to be compared under variation of the specific TIMs at similar boundary conditions.

6.1. Experimental Setup

To gain optical access to both sides of the experimental test section (heatable front and cooling channels) and to simplify construction and modifications, a flat test section was designed. The basic cooling channel geometry, as well as the aluminum base thickness and height, were the same as in a 16" wheel hub motor. The length of the test section is approximately 1/5th of the motor's circumference. In Figure 10a, the basic setup and the included parts of the demonstrator test section are shown. Figure 10b additionally depicts that the later introduced numerical model owns the identical geometry as the experimental demonstrator. The elongated inlet and outlet represent an exception, due to reasons of convergence. Figure 11 gives a deeper insight into the geometrical dimensions of the test section. In the frontal view (Figure 11a) the measurement section and the cross-section of the CCs are displayed. The side view (Figure 11b) shows the material thicknesses of the layered structure.

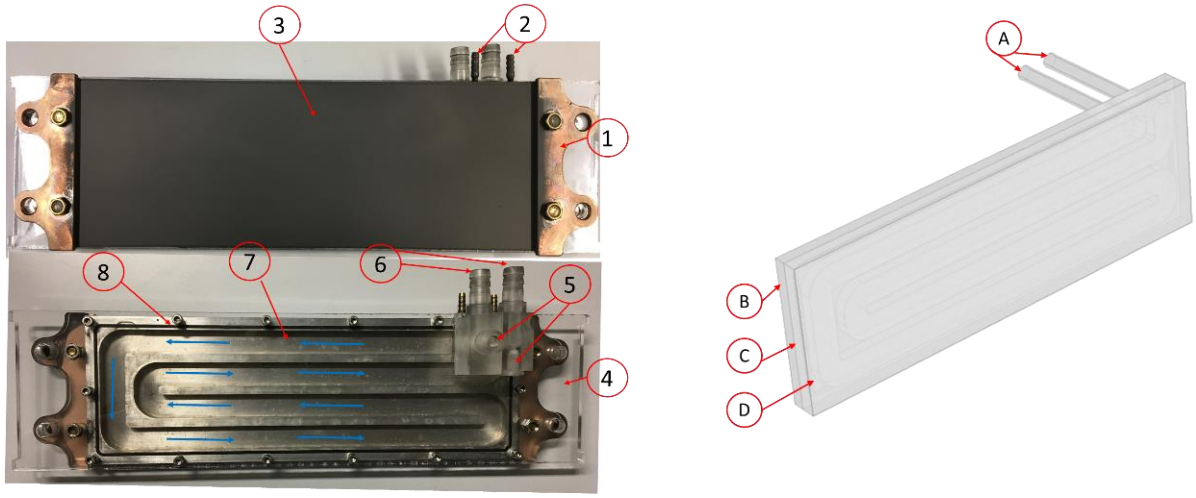


Figure 10. (**a**) Stator test section (top: 1—copper connectors, 2—tappings for pressure meas., 3—blackened Inconel® surface, bottom: 4—acrylic glass, 5—tappings for temp. meas., 6—in- and outlet, 7—cooling duct, 8—aluminum base); (**b**) flat stator test section FEM-model based on CAD data (A—abstracted and elongated inlet and outlet for stable convergence, B—acrylic glass, C—aluminum base with coolant ducts, D—100 µm Inconel® sheet).

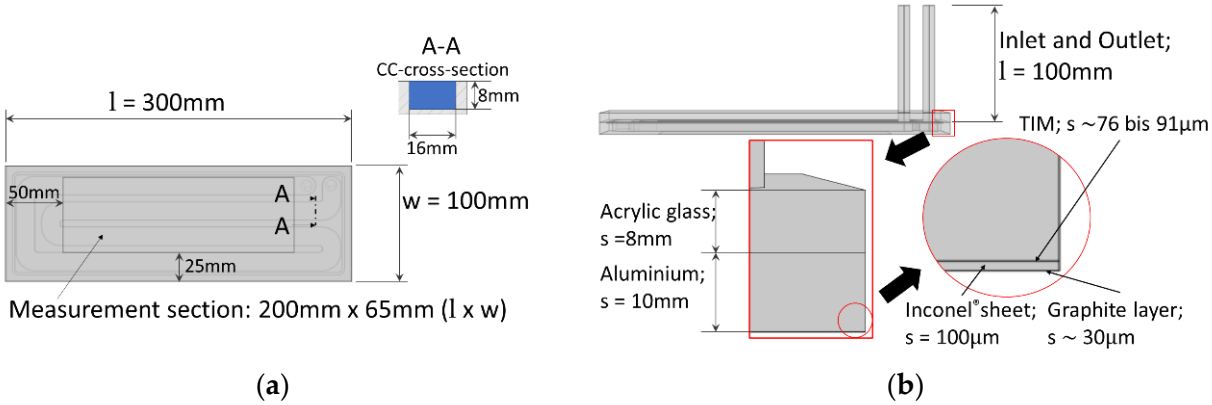


Figure 11. (**a**) Frontal view of the flat test section with dimensional data; (**b**) side view of the flat test section with the structure of the layering and corresponding thicknesses s.

To recreate the meander winding as the major heat source, a 100 µm Inconel®625 sheet was applied instead. Due to the minor temperature dependency of the specific electrical resistance of Inconel®, the boundary condition of constant heat flux can be realized more easily. The sheet was electrically insulated to the aluminum base, applying the TIM to be investigated. An infrared thermography camera measured the surface temperatures of the electrically heated Inconel®625 sheet. The applied mid wavelength system, IR8300 by InfraTec, has an optical resolution of 532 × 640 pixels and can resolve temperature differences of 25 mK. A high surface emissivity is essential for an accurate temperature acquisition by IR systems, which was achieved by blackening the surface with graphite.

The ohmic heating of the test section was realized by two parallel-connected Delta Elektronika SM15-200 power supplies, coupled to the Inconel® sheet by massive copper connectors. Considering the motor's ohmic losses, a heat flow of up to 1.6 kW could be achieved at the maximum.

The cooling fluid inlet and outlet were arranged in a rectangular bending with a connection for temperature probes. The tappings for the pressure sensors were directly connected to the fluid channels.

Hydraulic and temperature characteristics were covered via a variety of sensors installed in the system. Here, differential pressure Δp was additionally measured for reasons of validation to the numerical model. The differential pressure between inlet and outlet was measured by means of a Yokogawa EJX110A sensor. The mass flow rate was measured by means of a Krone Optimas MFS7000T06 Coriolis mass flow meter. The coolant temperature difference was measured using calibrated PT100 sensors. All data were logged using a National Instruments data acquisition system. A thermostat/cryostat ensured a constant inlet temperature. For high thermal loads, a water-cooled heat exchanger was added to the coolant circuit as a heat sink. The setup is shown in Figure 12.

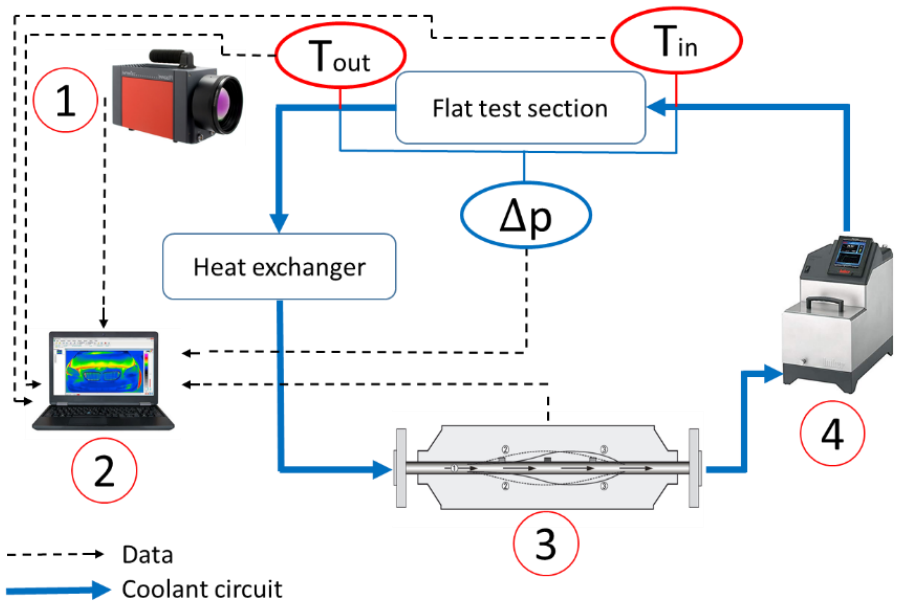


Figure 12. Schematic drawing of the test setup (1—thermographic imaging system, 2—data logging and control, 3—mass flow meter, 4—thermostat/cryostat).

The design of experiments (DoE) [35] method was applied to systematically plan the experiments. All TIMs from Table 1 were applied two times, for reasons of reproducibility. According to the DoE plan, heat and mass flow rates were varied in the range of $\dot{Q}$ =100–1200 W and $\dot{m}$ = 65–108 g/s, respectively. These variations embody a realistic range regarding the full motor application.

According to the DoE method, all input parameters, as shown in Figure 13, should be randomized. Randomization of the heat and mass flow rates was easy to realize. Regarding the interchangeability of the TIM, this was not the case at all. Randomization was not possible because each test was based on the same aluminum base body, and changing the TIM is a destructive process. To minimize external influences, the water inlet temperature, as well as the lab temperature, were kept constant at 25 °C.

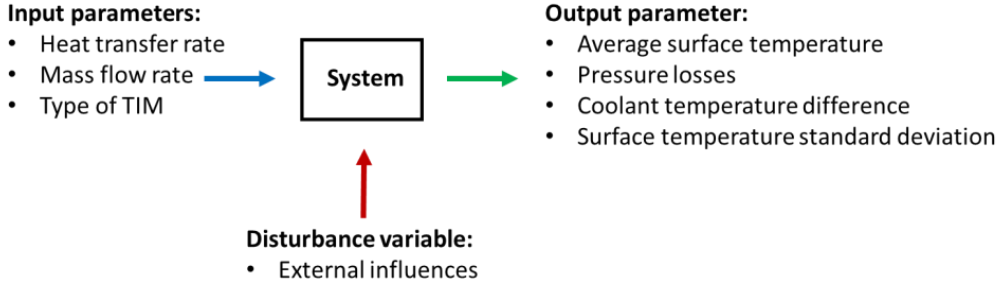


Figure 13. Parameter for DoE.

Figure 14 shows two exemplary results of the infrared thermographic investigations. In each case, TIM 2 is attached, under otherwise identical operating conditions. It is quite evident that the detected surface temperatures strongly depend on the quality of the film application. Thus, air pockets probably occurred in the 2nd application, whereupon partial hotspots can be found. Additionally, the edge areas show non-reproducible temperature characteristics due to the electric connectors.

To account for this, measurement sections were defined for further evaluation, see Figures 11a and 14, in form of rectangles (R1). Within this rectangle, the mean surface temperature $\overline{T}_{surf}$ and the standard deviation of the surface temperature $\sigma(\overline{T}_{surf})$ were determined.

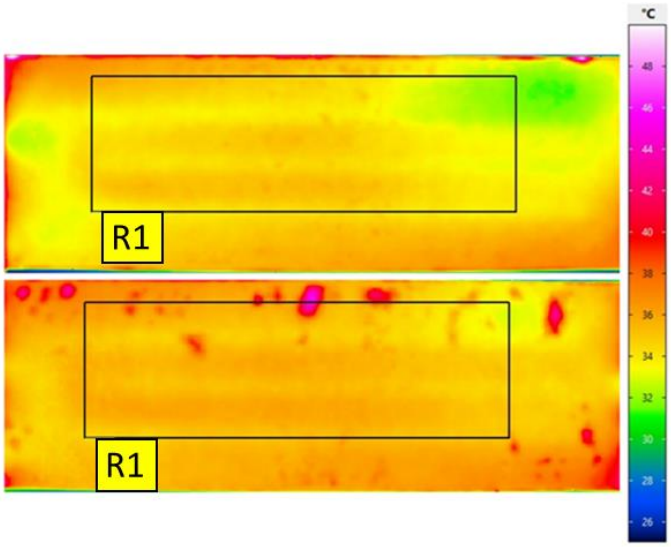


Figure 14. Surface temperature under application of TIM 2 with rectangular (R1) measurement section, (**top**) 1st tape application, (**bottom**) 2nd tape application.

As can be seen in Figure 15, there are only slight differences in the average surface temperature, depending on the TIM and the tape application. The scatter of the surface temperature increases slightly with the 2nd tape application, but this has no significant influence on the average surface temperature. The tendential effect of the TIMs is recognizable in both tape applications which indicates reproducible test conditions.

Since the effects are relatively small, as can be seen in Figure 15, a statistical test evaluation is useful for deriving reliable statements. Thus, the test plan can now be worked through in the following.

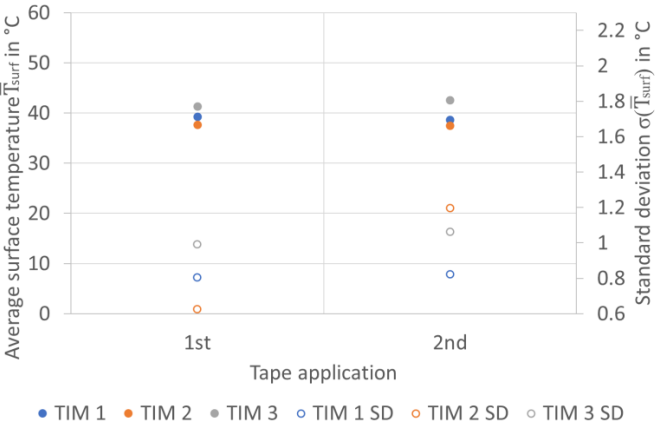


Figure 15. Variation of the measured values depending on the tape application.

6.2. Numerical Setup

To back up the experiments and determine further results regarding the deviations caused by the TIM application, a numerical study applying the finite elements method was conducted. For a detailed analysis of the heat and fluid flow in complex geometries, the finite element method is well-established. Comsol Multiphysics® 5.4 was applied in this study.

Importing the test section geometry directly from CAD into the FEM environment usually leads to bad convergence because data become inaccurate or even get lost in the transformation process. Therefore, a repairing process is necessary, in which the geometry is abstracted and convergence is improved. Short edges or narrow and sliver-like faces unnecessarily bind small and skewed mesh elements, resulting in a low-quality mesh. Defeaturing reduces the mesh elements and rises the mesh quality. However, the systems' heat and mass transfer-related properties must not be influenced too much. Regarding the abstractions, a good balance has to be found between accuracy on the one hand and required calculation time and power on the other hand.

Further model simplification includes the utilization of symmetries and dimensionality reduction of critical system properties [36]. Additionally, homogenization of heterogenous domains and properties is widely used [37].

In the numerical model, the fluid and heat transports were computed in conjunction.

The inlet and outlet were elongated to 100 mm to achieve a more stable convergence. Although the fluid regime in the coolant ducts should be laminar due to their Reynolds numbers, a turbulent regime must be considered in the elbows and the inlet and outlet. The shear stress transport (SST) model, which combines the k-ε and k-Ω models, was applied because it serves well for simultaneously computing near-wall effects (heat transport) and free flow [38]. A mass flow rate at the inlet and a constant pressure at the outlet were chosen as boundary conditions. All internal wall surfaces were considered hydraulically smooth.

As the maximum temperature of the heated Inconel® was kept below 60 °C and the temperature difference of the cooling water at the inlet and outlet was kept below 5 K, the temperature dependencies of the thermal–physical properties were neglectable. To minimize the computation time at each parameter variation, the thermal–physical properties, as shown in Table 5, were kept constant.

Table 5. Thermal–physical properties as applied in the FEM simulations.

Material	Heat Capacity in J/(kgK)	Density in kg/m^3	Th. Conductivity in W/(mK)
Acrylic	1420	1190	0.19
Aluminum	900	2700	190
Inconel®	496	8770	12.4
Water	4200	1000	0.6

To model the ohmic losses, the windings were assumed as a 100 µm thin volumetric heat source with up to 533 $\times$ 10^6 W/m^3 to emulate a maximum heat transfer rate of 8 kW for the motor in total at the stator-winding-surface.

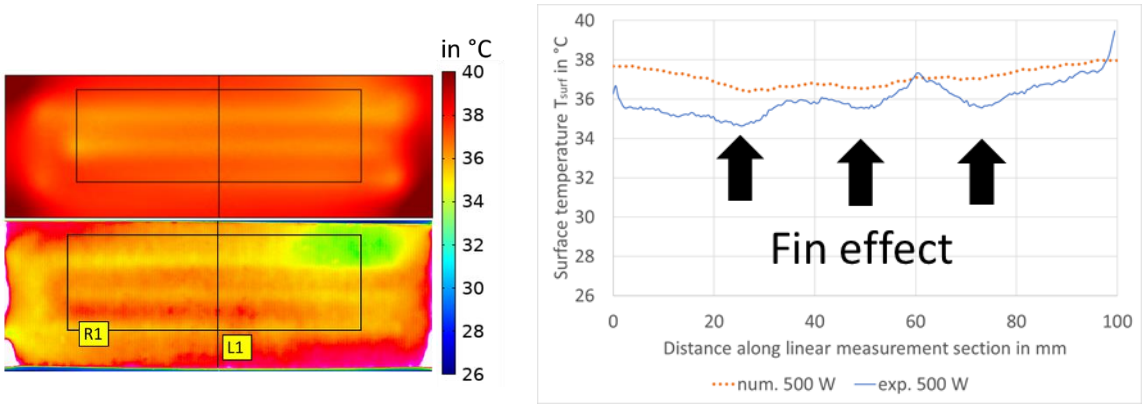
For the heat transport at the outer surfaces, free convection, as well as radiative heat transfer to the environment were modeled with a combined heat transfer coefficient of h_{comb} = 15 W/(m^{2}K).

The TIM between the Inconel® and the aluminum base was computed as a thermally thick layer to simplify meshing. The thermal conductivity of the respective TIMs was implemented based on the experimental evaluation, see Section 5. The thickness was based on the measurements in the applied state of the three-layer analysis. We implemented thicknesses of s_{TIM1} = 76 µm, s_{TIM2} = 80 µm, and s_{TIM3} = 91 µm, respectively.

Due to the insignificant temperature dependency of the effective thermal conductivity, constant values were taken at a temperature of 50 °C. This temperature level fit the achieved range of the experimental results well. Here, the implemented values were $k_{eff,TIM1}$ = 0.183 W/(mK), $k_{eff,TIM2}$ = 0.234 W/(mK), and $k_{eff,TIM3}$ = 0.160 W/(mK).

7. Comparative Analysis and Discussion

A comparison of experimental and numerical analyses in Figure 16a, under similar boundary conditions, indicates a high degree of qualitative agreement, although the absolute temperature level of the experimental results is slightly lower than that of the numerical results. Deviations only occur at the left and right edges where the electrical connections are located and in the area of the fluid inlet and outlet in the upper right area.



(**a**) (**b**)

Figure 16. (**a**) Comparison of numerical (top) and experimental (bottom) results with rectangular (R1) and linear (L1) measurement section, TIM 1, heat transfer rate $\dot{Q}$ = 500 W, mass flow rate $\dot{m}$ = 108 g/s, inlet temperature T_{in} = 25 °C; (**b**) numerical and experiment temperatures along linear measurement section L1.

Interestingly, slightly higher surface temperatures can be found in areas of the flow channel compared to areas that can be assigned to a wall between two channels. This does not seem plausible at first, but it is quite understandable if one considers that these walls have a kind of fin effect, whereby additional heat can be supplied to the cooling medium, see Figure 16a. This indicates the potential for further cooling channel modification utilizing fins and turbulators, and it also shows that the fin width is another optimization parameter. This matter has been extensively examined in another article [34].

In Figure 16b, the experimentally and numerically determined surface temperatures along the linear measurement section L1 are presented. Here, a distance of 0 mm corresponds to the position next to the inlet and outlet. A maximum temperature difference of approximately ΔT = 2 K can be observed next to the inlet and outlet region (0–30 mm). The suspicion intensifies, that numerically the heat transfer potential of the turbulent flow in the inlet/outlet region is underestimated. The middle section, as well as the opposite side, show even better quantitative agreement with the experimental results (ΔT~1 K). In addition, the fin effect can be observed at a distance of 25 mm, 50 mm, and 75 mm, leading to reduced local temperatures. It is more pronounced in the experimental results. Generally, both methods, the experiment as well as the numerical values show good qualitative and quantitative agreement. Due to their independence from each other, valid results seem probable.

Figure 17 shows the cooling water temperature difference as a function of the heat transfer rate at a constant mass flow rate of 86.5 g/s. Neglecting free convection and thermal radiation, the different TIM types do not affect the cooling water temperature difference, so only a dotted line is shown for numeric results in Figure 17. The numerical trend of the cooling water temperature difference ΔT_{cool} agrees with those of the experimental results.

The absolute uncertainty in the determination of the cooling water temperature difference is 0.14 K and results from the uncertainties of the individual PT-100 sensors. The uncertainty of the heat transfer rate is given in Figure 17, which also includes uncertainties of the mass flow sensor.

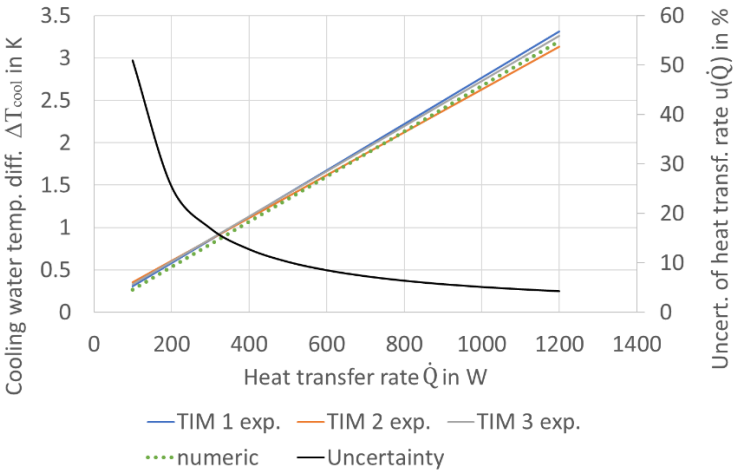


Figure 17. Cooling water temperature rise at different heat transfer rates, experimentally and numerically, $\dot{m}$ = 86.5 g/s, T_{in} = 25 °C.

Figure 18 shows the mean surface temperature as a function of the mass flow rate at a constant heat transfer rate of 650 W. The trend of the numerical and experimental curves is approximately the same. They both show slightly negative gradients with increasing mass flow rate. An increase in the mass flow rate leads to only marginal decreases in the mean surface temperature for all TIMs investigated. The deviations of the tapes are achieved in terms of the trend by both numerical values and experiments, i.e., TIM 2 has the lowest surface temperature, followed by TIM 1 and TIM 3. These trends are due to the different thermal resistances of the tapes, as shown in Section 5. It is also noticeable here that the mean surface temperature has a slight offset. For the TIM types, the offset between numerics and experiments is about 2–3 K for a mass flow rate of 108 g/s in each case. The relative uncertainty of the mass flow rate, provided in the manufacturer's specifications, is also given in Figure 18. For the surface temperature determined by means of infrared thermography, an absolute uncertainty of 1.2 K to 1.4 K could be calculated, which is due to inaccuracies in the determination of the emissivity.

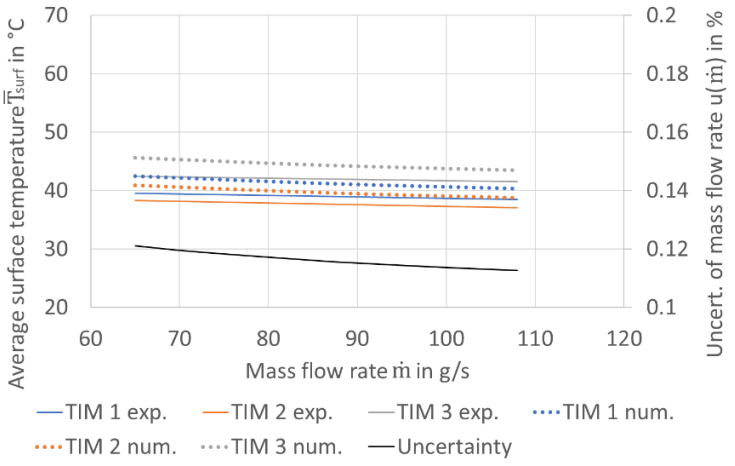


Figure 18. Influence of mass flow rate on average surface temperature for different TIMs, $\dot{Q}$ = 650 W, T_{in} = 25 °C.

The mean surface temperature as a function of the heat transfer rate is plotted in Figure 19, at a constant mass flow rate of 86.5 g/s for the investigated TIMs. The heat transfer rate has a significant impact on the surface temperatures and, thus, on the thermal limitations of the electrical machine. Additionally, the influence of the selected TIM can be observed so that in the investigated area, the average surface temperature can be reduced by up to 8 K, using TIM 2 compared to TIM 3. It proves that a thicker Kapton® MT+ layer with simultaneous reduction of the adhesive layer leads to an improved heat transfer behavior, see TIM 1 and TIM 2 in Table 1. Comparing the numerical and the experimental values, it is noticeable that the results of the numerical values show higher slopes. In the case of TIM 1 and 2, the differences in the mean surface temperatures between the experiments and the numerical values are about 4 K for a heat transfer rate of 1200 W. TIM 3 shows a difference of about 5 K.

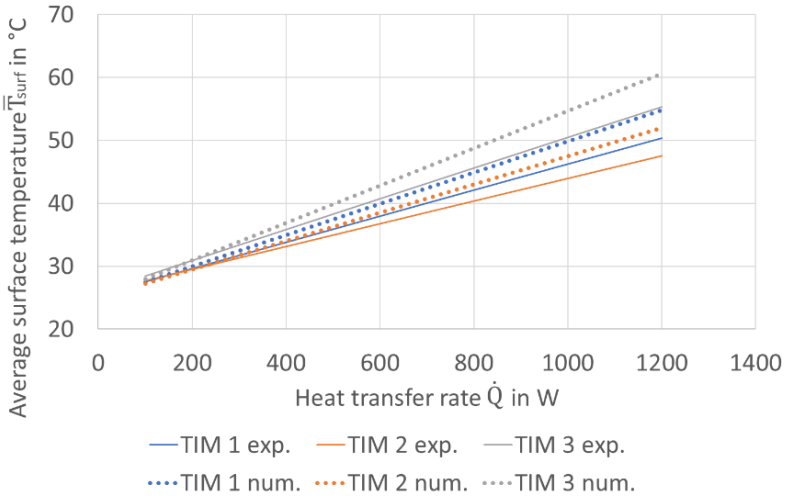


Figure 19. Effect of the heat transfer rate on the mean surface temperature, $\dot{m}$ = 86.5 g/s, T_{in} = 25 °C.

The systematic differences between the numerical and the experimental investigations can be well explained by the heat transfer coefficients on the fluid side. The determined heat transfer coefficients in the numerical investigations were predicted to be somewhat too low so that slightly higher surface temperatures occurred in the numerical investigations compared to the experimental results. The simulation assumes completely smooth channel walls, whereas, in reality, the manufacturing of the channels can result in microscopic scratches and bumps, that influence and intensify flow micro turbulences near the wall and therefore the effective heat transfer.

8. Summary and Outlook

In this paper, the utilization of industrially manufactured PSA tapes as a novel form of TIM is investigated. The suitability of three differently composed TIMs is tested to reduce the thermal load in a compact electrical machine with air-gap winding. These TIMs must have robust adhesive properties to ensure a reproducible manufacturing process and a reliable interface connection throughout the operating lifetime. Additionally, there are contradictory requirements, such as sufficient electrical insulation combined with low thermal resistance. The TIMs' multi-physical material properties are investigated and compared, both experimentally and numerically. All performed analyzes are applied to the subsequent requirements in the electric motor.

The adhesive strength of the TIM to the contacted surfaces, the winding on the one side, and the stator on the other side was tested at operating temperatures of up to 130 °C. The strength requirements were met by TIM 1 and TIM 3. However, TIM 2, which is coated with a filled polysiloxane-based adhesive coating on the stator side, required a pre-treatment with a primer.

Thermal–physical property examinations included LFA in combination with DSC. The LFA measurements result in an effective thermal conductivity, including every contact resistance. To account for the application, the dependency on temperature and surface roughness was examined. Considering the total measured thickness of the TIM in the applied state, the thermal resistance was calculated. The results showed a significant influence of the surface roughness. The compound of thin, highly viscous adhesive and hard Kapton® carrier led to insufficient wetting of the rougher adjacent contact surface. The total thermal resistance increased up to 100%, compared to smooth surfaces.

Applying a flat test section to emulate engine-like conditions, the influence of the thermal-physical properties of the TIMs on the heat dissipation capability was examined. Therefore, a comparative numerical and experimental study was performed. The surface temperature of the flat test section was determined via infrared thermography. Here, a lower average temperature indicates a better performance of the TIM in terms of lower thermal resistance. The winding of the real motor was replaced by an ohmic heated Inconel® sheet. Changes in the surface temperature can be compared under the variation of heat transfer rate, the mass flow rate of the coolant, and the specific TIMs at similar boundary conditions.

It is shown that the adjusted mass flow rate had no significant influence on the surface temperature. Only a small temperature difference of approximately 2 K for the respective TIM type was measurable as the mass flow rate was increased from 65 g/s to 108 g/s at a constant heat transfer rate of 650 W. This influence was also confirmed by the numerical simulations, in which the measured thermal–physical properties were implemented.

The variation of the heat transfer rate on the mean surface temperature was more significant. At a constant mass flow rate of 86.5 g/s, a temperature increase, up to 26 K, was detectable in the experiments. Numerically, this trend was confirmed.

For TIM 2, which has the lowest thermal resistance of all TIMs investigated, the lowest mean surface temperature was demonstrated, both numerically and experimentally. At the highest investigated thermal load, a reduction of the surface temperature of about 8 K compared to TIM 3 could be shown experimentally. With 9 K, this tendency was slightly overpredicted by the numerical simulation.

Future research is necessary to enhance the performance potential of these electric drives.

The experimental and numerical investigations on the flat test section, carried out in this article, revealed further optimization potential to reduce the system's total thermal resistance. A modified cooling channel geometry with implemented fins and turbulators, realized with additive manufacturing methods, appears desirable in combination with real motor tests.

To investigate the aging behavior of the PSA tapes, thermogravimetric investigations on differently aged samples could be performed and supported by mechanical stress analysis. Respecting this, also repetition of the application tests with the real motor appears to be useful.

Further systematical investigations of these TIMs, regarding the influence of the adhesive layer thickness on the effective thermal resistance, have to be carried out. In this context, a variation of the roughness of adjacent materials, temperatures, and contact pressure depending on the adhesive formulations of the TIMs seems reasonable.

Author Contributions: Conceptualization, H.-C.G., J.S. and G.B.; methodology, H.-C.G., J.S. and G.B.; software, H.-C.G., J.S. and G.B.; validation, H.-C.G. and G.B.; formal analysis, H.-C.G. and G.B.; investigation, H.-C.G., J.S., O.S. and G.B.; resources, F.B.; data curation, H.-C.G. and G.B.; writing—original draft, H.-C.G., J.S., O.S. and G.B.; writing—review and editing, H.-C.G., J.S. and G.B.; visualization, H.-C.G., O.S. and G.B.; supervision: J.S, G.B. and F.B.; project administration, J.S, F.B. and G.B.; funding acquisition, J.S. and F.B. All authors have read and agreed to the published version of the manuscript.

Funding: This publication was realized within the framework of the joint project Kompetenzzentrum eMobility and was funded by European Regional Development Fund (ERDF) and the state of Saxony-Anhalt, grant number ZS/2018/09/94406.

Acknowledgments: The authors would like to thank CMC Klebetechnik GmbH for their cooperation and for providing the Thermal Interface Materials as well as S. Horn for supporting the investigations within his master thesis. We acknowledge support for the Book Processing Charge by the Open Access Publication Fund of Magdeburg University.

Conflicts of Interest: The authors declare no conflict of interest.

Nomenclature

Abbreviation		
$\sigma(x)$	standard deviation of measured value x	respective to measured value x
ρ	density	kg/m^3
A	area	m^2
B	magnetic flux density	T
BLT	bond line thickness	µm
c	specific heat capacity	J/(kgK)
C	confidence interval	%
D	thermal diffusivity	m^2/s
F	force	N
h	heat transfer coefficient	$W/(m^2K)$
I	current	A
k	thermal conductivity	W/(mK)
l	length	m
$\dot{m}$	mass flow rate	kg/s
p	pressure	Pa
Δp	differential pressure	Pa
$\dot{q}$	heat flux	W/m^2
$\dot{Q}$	heat transfer rate	W
r	thermal resistance	$(m^2K)/W$
R	roughness value	µm
s	thickness	m
T	temperature	°C
$\overline{T}$	mean temperature	K
ΔT	temperature difference	K
u	unit of heat transfer	$W/(m^2K)$
u(x)	uncertainty of measured value x	%
w	width	m

Subscripts		**Acronyms**	
a	average	BLT	bond line thickness
adh, 1, 2	adhesive layer 1, 2	CAD	Computer-Aided-Design
Al	aluminum	CC	cooling channel
cd	cooling ducts	DoE	Design of Experiment
c1, 2	contact at interface 1, 2	DSC	Differential Scanning Calorimetry
c1, 2, TIM	contact at interface 1, 2 inside TIM	ESU	Equipment Specific Uncertainty
comb	combined	FEM	Finite Element Method
cool	cooling water	IR	infrared
eff	effective	LFA	Laser Flash Analysis
in	inlet	LMA	low melting alloy
L	Lorentz	MSU	Model Specific Uncertainty
max	maximum	PCM	Phase Change Material
min	minimum	PSA	Pressure-Sensitive Adhesive
out	outlet	RTD	resistance temperature detector
pi	polyimide	SST	Shear Stress Transport
surf	surface	SSU	Sample Specific Uncertainty
TIM (1,2,3)	Thermal Interface Material (1,2,3)	TIM	Thermal Interface Material
th	thermal		

References

1. Zörnig, A.; Kasper, R. Konstruktion elektrischer Radnabenmotoren mit Luftspaltwicklung für Kraftfahrzeuge. *Konstruktion* **2015**, *6*, 40–43. [CrossRef]
2. Kasper, R.; Borchardt, N. Boosting power density of electric machines by combining two different winding types. *IFAC-PapersOnLine* **2016**, *49*, 322–329. [CrossRef]
3. Greenwood, J.A.; Williamson, J.B.P. Contact of normally flat surfaces. *Proc. R. Soc. Lond.* **1966**, *295*, 300–319. [CrossRef]
4. Yovanovich, M.M. Four decades of research on the thermal contact, gap, and joint resistance in microelectronics. *IEEE Trans. Compon. Packag. Technol.* **2005**, *28*, 182–206. [CrossRef]
5. Prasher, R. Thermal Interface Materials: Historical perspective, status, and future directions. *Proc. IEEE* **2006**, *94*, 1571–1586. [CrossRef]
6. Sarvar, F.; Whalley, D.C.; Conway, P.P. Thermal Interface Materials—A review of the state of the art. In Proceedings of the 1st Electronic System Integration Technology Conference, Dresden, Germany, 5–7 September 2006; pp. 1292–1302. [CrossRef]
7. Tong, X.C. *Advanced Materials for Thermal Management of Electronic Packaging*, 1st ed.; Springer: New York, NY, USA, 2011; pp. 305–371.
8. Otiaba, K.C.; Ekere, N.N.; Bhatti, R.S.; Mallik, S.; Alam, M.O.; Amalu, E.H. Thermal interface materials for automotive electronic control unit: Trends, technology and R&D challenges. *Microelectron Reliab.* **2011**, *51*, 2031–2043. [CrossRef]
9. Pathumudy, R.D.; Prabhu, K.N. Thermal Interface Materials for cooling microelectronic systems: Present status and future challenges. *J. Mater. Sci. Mater. Electron.* **2021**, *32*, 11339–11366. [CrossRef]
10. Bahru, R.; Zamri, M.F.; Shamsuddin, A.H.; Shaari, N.; Mohamed, M.A. A review of Thermal Interface Material fabrication method toward enhancing heat dissipation. *Int. J. Energy Res.* **2020**, *45*, 3548–3568. [CrossRef]
11. Grujicic, M.; Zhao, C.L.; Dusel, E.C. The effect of thermal contact resistance on heat management in the electronic packaging. *Appl. Surf. Sci.* **2005**, *246*, 290–302. [CrossRef]
12. Gwinn, J.P.; Saini, M.; Webb, R.L. Apparatus for accurate measurement of interface resistance of high performance Thermal Interface Materials. In Proceedings of the 8th Intersociety Conference on Thermal and Thermomechanical Phenomena in Electronic Systems, San Diego, CA, USA, 30 May–1 June 2002; pp. 644–650. [CrossRef]
13. Cui, Y.; Li, M.; Hu, Y. Emerging interface materials for electronics thermal management: Experiments, modeling, and new opportunities. *J. Mater. Chem. C* **2020**, *8*, 10568–10586. [CrossRef]
14. Zhao, J.-W.; Zhao, R.; Huo, Y.-K.; Cheng, W.-L. Effects of surface roughness, temperature and pressure on interface thermal resistance of Thermal Interface Materials. *Int. J. Heat Mass Transf.* **2019**, *140*, 705–716. [CrossRef]
15. Blazej, D. Thermal Interface Materials. Available online: https://www.electronics-cooling.com/2003/11/thermal-interface-materials/ (accessed on 18 January 2022).
16. Viswanath, R.; Wakharkar, V.; Watwe, A.; Lebonheur, V. Thermal performance challenges from silicon to systems. *Intell. Technol. J.* **2000**, *3*, 1–16.
17. Eveloy, V.; Rodgers, P.; Pecht, M.G. Reliability of pressure-sensitive adhesive tapes for heat sink attachment in air-cooled electronic assemblies. *IEEE Trans. Device Mater. Reliab.* **2004**, *4*, 650–657. [CrossRef]
18. Lin, S.B.; Durfee, L.D.; Ekeland, R.A.; McVie, J.; Schalau, G.K. Recent advances in silicone pressure-sensitive adhesives. *J. Adhes. Sci. Technol.* **2007**, *21*, 605–623. [CrossRef]
19. Epple, T.C. Pressure-Sensitive Tape Solutions for Electronics. Available online: https://www.adhesivesmag.com/articles/97851-pressure-sensitive-tape-solutions-for-electronics (accessed on 30 January 2022).
20. Krusinski, S. Solving Challenges in Electric Vehicle Batteries with Pressure-Sensitive Tapes. Available online: https://www.adhesivesmag.com/articles/98760-solving-challenges-in-electric-vehicle-batteries-with-pressure-sensitive-tapes (accessed on 30 January 2022).
21. Lee, Y.J. Thermally conductive adhesive tapes—A critical evaluation and comparison. *Adv. Packag.* **2007**, *16*, 28–30.
22. Chu, H.; Selvakumar, A. Performance characterization of pressure sensitive adhesive Thermal Interface Materials. In Proceedings of the 25th Annual IEEE Semiconductor Thermal Measurement and Management Symposium, San Jose, CA, USA, 15–19 March 2009. [CrossRef]
23. Novák, I.; Florián, Š. Pressure-sensitive adhesives for electronic applications. *J. Mater. Sci. Lett.* **2003**, *22*, 1237–1239. [CrossRef]
24. Chirtoc, M.; Chirtoc, I.; Pittois, S.; Glorieux, C. Thoen Thermal resistance of adhesive tapes measured by the photopyroelectric method. *Rev. Sci. Instrum.* **2003**, *74*, 632–634. [CrossRef]
25. Hienonen, R.; Keskinen, J.; Koivuluoma, T. *Reliability of Materials for the Thermal Management of Electronics*; VTT Publications No. 619; VTT Technical Research Centre of Finland: Espoo, Finland, 2006; pp. 1–149. Available online: http://www.vtt.fi/inf/pdf/publications/2006/P619.pdf (accessed on 30 January 2022).
26. Demko, M.T.; Yourey, J.E.; Wong, A.; Lin, P.-Y.; Blackman, G.S.; Catlin, G.C.; Yahyazadehfar, M. Thermal and mechanical properties of electrical insulating Thermal Interface Materials. In Proceedings of the 16th IEEE Intersociety Conference on Thermal and Thermomechanical Phenomena in Electronic Systems (ITherm), Orlando, FL, USA, 30 May–2 June 2017; pp. 237–242. [CrossRef]
27. Von Böckh, P.; Wetzel, T. Wärmeleitung in ruhenden Stoffen. In *Wärmeübertragung—Grundlagen und Praxis*, 7th ed.; Springer Vieweg: Berlin/Heidelberg, Germany, 2017; pp. 17–27.

28. Chiu, C.-P.; Solbrekken, G.L.; Chung, Y.D. Thermal modeling of grease-type interface material in PPGA application. In Proceedings of the Thirteenth Annual IEEE Semiconductor Thermal Measurement and Management Symposium, Austin, TX, USA, 28–30 January 1997. [CrossRef]
29. Brockmann, W.; Geiß, P.L.; Klingenberg, J.; Schröder, B. *Klebtechnik: Klebstoffe, Anwendungen und Verfahren*, 1st ed.; Wiley-VCH: Weinheim, Germany, 2008.
30. Frederici, G. Wärmeleitende Produkte für die Elektronik—passiv und aktiv. *Electron. Fab* **2017**, *2*, 76–78.
31. Stamann, O.; Jüttner, S.; Sauerhering, J.; Zörnig, A.; Kasper, R. Untersuchung von doppelseitig klebenden Elektroisolierfolien mit wärmeleitfähigen Klebstoffschichten zum Fügen der Luftspaltwicklung von Leichtbau-Elektroantrieben. *MMT* **2019**, *14*, 162–171. [CrossRef]
32. Casalegno, V.; Vavassori, P.; Valle, M.; Ferraris, M.; Salvo, M.; Pintsuk, G. Measurement of thermal properties of a ceramic/metal joint by laser flash method. *J. Nucl. Mater.* **2010**, *407*, 83–87. [CrossRef]
33. Hohenauer, W.; Vozár, L. An estimation of thermophysical properties of layered materials by the laser-flash method. *High Temp.-High Press.* **2001**, *33*, 17–25. [CrossRef]
34. Graichen, H.-C.; Sauerhering, J.; Reuber, F.; Dlugosch, A.; Chinni, M.; Beyrau, F.; Boye, G. Advanced thermal management optimization of a liquid-cooled compact electrical engine with air gap winding. In Proceedings of the FISITA 2021 World Congress, Prague, Czech Republic, 14–16 September 2021. [CrossRef]
35. Siebertz, K.; van Bebber, D.; Hochkirchen, T. *Statistische Versuchsplanung. Design of Experiments (DoE)*, 2nd ed.; Vieweg: Berlin/Heidelberg, Germany, 2017; pp. 27–32.
36. Jaeger, M.; Ruf, A.; Hameyer, K.; Grosse-von Tongeln, T. Thermal analysis of an electrical traction motor with an air cooled rotor. In Proceedings of the IEEE Transportation Electrification Conference and Expo (ITEC), Long Beach, CA, USA, 13–15 June 2018; pp. 467–470. [CrossRef]
37. Queisser, O.; Cloos, L.; Boehm, F.; Oehler, D.; Wetzel, T. Impact of the level of homogenization in 3D thermal simulation on the internal temperature distribution of Li-ion battery cells. *Energy Technol.* **2021**, *9*, 2000915. [CrossRef]
38. Menter, F.R.; Kuntz, M.; Langtry, R. Ten Years of Industrial Experience with the SST Turbulence Model. *Turbul. Heat Mass Transf.* **2003**, *4*, 625–632.